05

Electropulse („spark“) plasma sintering of tungsten and W+5%Ni nanopowders obtained by high-energy ball milling

© E.A. Lantsev, N.V. Malekhonova, A.V. Nokhrin, K.E. Smetanina, A.A. Murashov, G.V. Shcherbak, A.V. Voronin, A.A. Atopshev

Lobachevsky University of Nizhny Novgorod,
603105 Nizhny Novgorod, Russia
e-mail: elancev@nifti.unn.ru, malekhonova@nifti.unn.ru

Received June 2, 2023
Revised September 2, 2023
Accepted September 21, 2023

The mechanisms of high-speed sintering of tungsten and W+5 wt.% Ni nanopowders obtained by high-energy ball milling (HEBM) have been studied. The phase composition, microstructure parameters, hardness and fracture resistance of the obtained samples were investigated. It is shown that the samples have high relative density, small grain size and increased hardness. It is established that the formation of strong intermetallic phases $Me_xW_yC_z$ and Me_xW_y, as well as MeO oxides occurs at SPS of mechanically activated nanopowders. The simultaneous increase in the content of intermetallic phases and reduction of the grain size leads to a non-monotone character of the dependence of the SPS activation energy on the HEBM time. It is shown that the main mechanism of SPS of tungsten W+5 wt.% Ni nanopowders is Coble creep.

Keywords: tungsten, mechanical activation, nanopowders, spark plasma sintering, density, grain size, diffusion.

DOI: 10.61011/TP.2023.11.57494.143-23

Introduction

Tungsten heavy alloys (THA) feature a combination of high strength and room-temperature plasticity [1,2], high radiation resistance and other properties. Commercial tungsten alloys with 90−95% W, produced by the conventional liquid phase sintering method have a density of 17−19 g/cm^3, tensile strength up to 1000 MPa and elongation up to 25−30% at room temperature. Additional strain hardening improves the tensile strength up to 1400−1600 MPa while maintaining the adequate plasticity [3].

Traditional THA strain hardening processes have achieved their capability limits by now and modern powder metallurgy technologies are frequently used for additional improvement of THA performance [4]. Modern tungsten-based nanopowder composition methods are being developed extensively [5] and new fine-grain THA sintering methods are being developed.

Spark „plasma“ sintering (SPS) process, a high-speed hot pressing method, is one of the promising THA production methods [6]. Capability of materials sintering at extra high heating rates (up to 2500°C/min) ensures reduction of the grain growth rate and production of high-strength and high-hardness fine-grain THA [7,8].

Simultaneous use of the high-energy mechanical activation (HMA) process and SPS ensures record-breaking increase in THA strength and hardness [9]. The findings of [10,11] show that HMA may result in formation of highly supersaturated nickel-based tungsten solid solution in the γ-phase and, thus, in some unexpected effects. The effect of non-monotonic dependences of density on sintering temperature [8,12] and the effect of nanopowder sintering activation energy reduction deserve particular attention. From a practical perspective, improvement of hardness, static and dynamic strength of THA produced by a combination of HMA and SPS is important [13,14].

Currently, pure tungsten and THA are being extensively investigated as promising materials for heat and radiation resistant components of the International Thermonuclear Experimental Reactor (ITER) that are in contact with plasma [15–17]. Since grain boundaries are the excessive defect drain, the developers believe that nano- and fine-grain THA with small Ni additive that has adequately high melting point and low neutron capture cross-section (radius) will be widely used in nuclear power (See, for example, [18]).

Attention shall be also paid to the effect of pseudo incomplete solid-phase nickel-wetting of tungsten grain boundaries found in [19]. This effect opens wide prospects for the development of high-performance solid-phase sintering of THA, whose main problem is in poor spreading (wetting) of tungsten grains by the solid γ-phase.

Thus, tungsten-based THA are promising materials for mechanical engineering and nuclear power applications, which is the basis of practical importance of this study. The objective of this study is to investigate the high-speed sintering processes in pure tungsten and W+5% Ni alloy samples, and to examine the microstructure parameters and stress-strain properties of the obtained samples.

1. Experimental setup description

Commercial tungsten powders and powder $\alpha-$W+5 wt.% Ni composition were used as test objects. Tungsten powders with mean particle sizes $3-5\,\mu$m and nickel powders with mean FSSS (Fisher sub-sieve sizer) size of $20\,\mu$m were used. Initial coarse-grain compositions were produced by mixing W and Ni powders in a standard biconical mixer. Mixing time was 15 h, mixing speed was 100 rev/min. HMA of W and W+5 % Ni powders was carried out in APF-3 (Russia) planetary mill. grinding bodies acceleration was 60 g, mixing speed was 1450 rev/min. The container and $\varnothing$10 mm grinding balls were made from ShH-15 steel. HMA with time 1, 5, 12 and 20 min was carried out in argon atmosphere with ethanol addition.

Cylindrical samples 8 g in weight, 12 mm in diameter and 5 mm in height were preliminary compacted using a steel mold. To remove excess oxygen absorbed on the nanoparticle surface, the compacted pieces were annealed in hydrogen at 900°C during 1 h. SPS of annealed compacted pieces was carried out using Dr. Sinter model SPS-625 unit. The samples were sintered in continuous heating mode at a rate of 25°C/min up to sintering temperature T_s followed by free-mode cooling. For heating, 12x3 ms DC current pulses were applied through the graphite mold with subsequent 2x3 ms pause. Holding at T_s was not used. Uniaxial pressure (70 MPa) was applied simultaneously with the start of heating. The temperature was measured by CHINO IR-AH optical pyrometer focused on the graphite mold surface. The temperature measurement accuracy was $\pm$20°C. effective powder shrinkage L_{eff} was recorded using Futaba Pulscale SMM151A dilatometer included in Dr. Sinter model SPS-625 unit. Empty mold heating experiment was carried out to consider the thermal expansion contribution. The true shrinkage value (L) was calculated as follows $L(T) = L_{\text{eff}}(T) - L_0(T)$.

Microstructure testing of powders and sintered samples was carried out using Jeol JSM-6490 scanning-electron microscope (SEM) with Oxford Instruments INCA 350 energy-dispersive microanalyzer. X-ray phase analysis (XRD) was carried out using Shimadzu XRD-7000 (CuK_α diffractometer, sampling interval 0.04°, point exposure time is 2 s). Qualitative phase analysis was performed in „Diffrac.EVA“.

Hardness of the sintered samples was measured using Qness A60+ hardness tester. Load was equal to 10 kg. Minimum fracture resistance (K_{IC}) was calculated by the maximum radial crack length using the Palmquist model. For K_{IC} calculation, the modulus of elasticity of tungsten and W+5% Ni alloy was taken equal to $E = 390$ and 372 GPa, respectively.

Before the microstructure and stress-strain testing, the sintered samples were ground and polished to remove the $\sim 300 - 350\,\mu$m carburized layer formed as a result of carbon diffusion from the graphite mold into the surface layer of the sample (see [20]).

2. Description of the experimental findings

Figure 1 shows electron microscopy images of W and W+5% Ni powders after various milling periods. Figure 1 shows that powders form $80-120\,\mu$m agglomerates that are gradually broken during milling. Each agglomerate after 20 min HMA contains 40−70 nm W nanoparticles (Figure 1, e).

Figure 2, *a* shows diffraction patterns of tungsten powders after various HMA times (1, 5, 12, 20 min), where only tungsten peaks are identified. Diffraction patterns of W+5% Ni powders (Figure 2, *b*) have nickel peaks only on the 1 min HMA diffraction pattern. In diffraction patterns of the powders subjected to long-term HMA, nickel peaks are not distinguished at the background. This may suggest intensive grinding of nickel particles and/or contamination of into tungsten particles with nickel particles during HMA of W+5% Ni powders. It is well known that the lower the mean power particle size the wider diffraction peaks (provided that the measurement conditions are maintained), therefore, the broadened diffraction peaks of Ni become indistinguishable when permanent Ni concentration in the mixture is maintained.

Figure 3 shows the curve of peak full width at half maximum (FWHM) vs. HMA time for diffraction peak (321) of tungsten (at $2\theta \approx 131.2°$). It is shown that FWHM increases with increasing HMA time in both cases, however, this increase is greater when there is nickel in the powder. This may indirectly indicate that contamination of tungsten particles with nickel particles is taking place during HMA of W+5% Ni powders.

Figure 4 shows temperature dependences of shrinkage L and shrinkage rate S of W (a, b) and W+5% Ni (c, d) powders. $S(T)$ for tungsten powders has a conventional two-stage behavior with its peak at $\sim$ 1100 °C (Figure 4, *b*). When the tungsten powder HMA time increases, displacement of typical compaction processes towards lower temperatures is observed. After HMA, the peak of $S(T)$is observed during 20 min at 930°C. At the same time, when the HMA time increases from 1 min to 20 min, sintering temperature decrease from 1220 to 1050°C is observed (Figure 4, *a*).

Dependence of shrinkage on heating temperature $S(T)$ for W−5% Ni powders has also two-stage behavior (Figure 4, *d*). It should be noted that the compaction kinetics behavior, $S(T)$ view and typical shrinkage end temperature do not depend on the HMA time of the powders. The end of shrinkage of mechanically activated W+5% Ni powders occurs at $\sim$ 1000°C (Figure 4, *c*). The powder with the maximum milling time (20 min) has the highest maximum shrinkage rate ($S_{\max} = 0.013$ mm/s).

Specifications of sintered tungsten and W+5% Ni alloy samples are listed in the Table showing that the SPS method provides high relative density ρ/ρ_{th} in tungsten-based samples. The density of the sintered pure tungsten samples is $\sim$ 96.5%, and nickel introduction into the

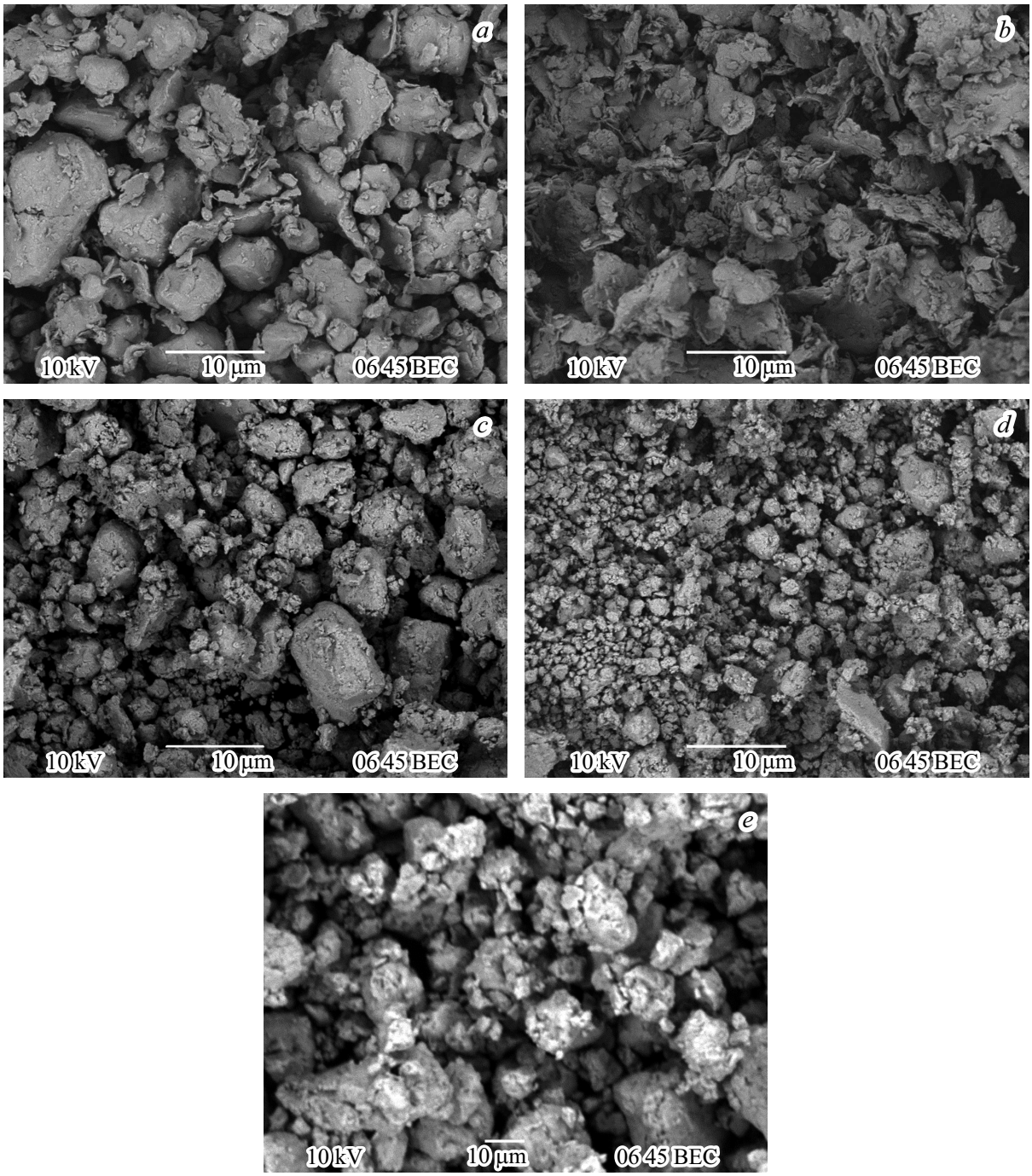

Figure 1. Electron microscopy images of W (a, b) and W+5% Ni ($c-e$) powders with various milling times: a, b — 1, $c-e$ — 20 min.

initial tungsten powder increases the relative density of the samples up to $\sim 99\%$.

Figure 5 shows the electron microscope analysis of fractures in sintered tungsten and W+5% Ni alloy samples. Figure 5 shows that the mean grain size in pure tungsten decreases from 7.5 μm to 0.8 μm when milling time increases from 1 min to 20 min (Figure 5, *a, b*). When the HMA time increases from 1 min to 20 min, the mean grain size of tungsten in W+5% Ni samples decreases from 1.8 μm to 0.3 μm (Figure 5, *c*).

XRD summary shows that carbide and intermetallic phases of $Me_xW_yC_z$ and Me_xW_y as well as MeO are formed during SPS (Figure 6, 7). We believe that this effect may be caused by contamination from steel balls and container during powder HMA.

Electron microscopy analyses of sintered sample this sections (Figure 8) show that considerable increase in the volume fracture of black regions in observed when the HMA time is increased. We believe that these regions refer to ternary carbides that are formed in these samples during

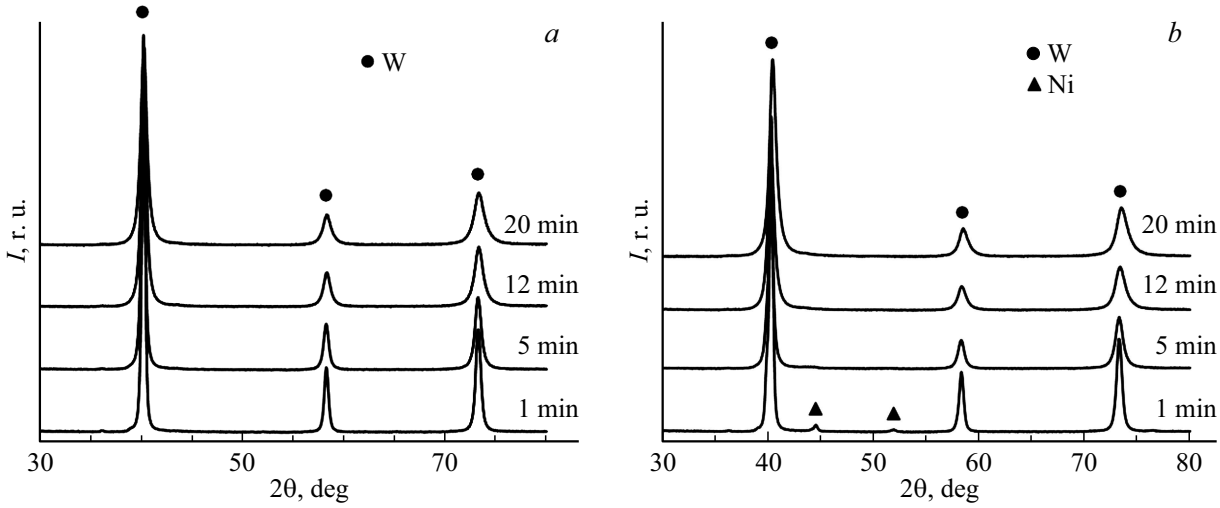

Figure 2. diffraction patterns of W (a) and W+5% Ni (b) powders after HMA. HMA times are specified.

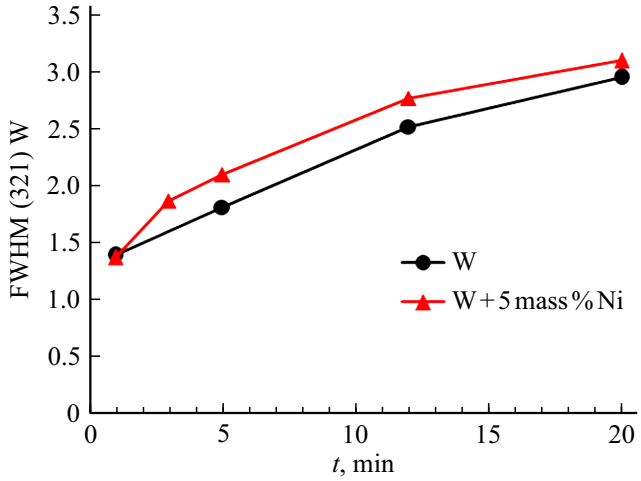

Figure 3. FWHM vs. HMA time for tungsten peak (321).

SPS, and this is in good agreement with the XRD data (Figure 6, 7). The largest individual particles are marked with arrows in Figure 8. Figure 8, d shows that, in the samples sintered from powders with long HMA times, carbide and intermetallic particles form 10−15 μm microstructure fragments that form a „cellular“ microstructure in some areas on the sample. In Figure 8, d, boundaries of such microstructure areas („cells“) are marked by a dashed line. Such 10−15 μm „cells“ contain tungsten grains that virtually have no coarse particles at their boundaries. With increasing HMA time, the amount of fully formed „cells“ increases and their size decreases;decrease in size of individual carbide and intermetallic particles is also observed.

Analysis of the data listed in the Table shows that the tungsten samples have a hardness of $H_v = 3.9$ GPa and a fracture resistance of 5.1 MPa·m$^{1/2}$ with HMA time increasing from 1 min to 20 min, the tungsten sample hardness increases from 3.9 GPa to 6.5 GPa. When 5% Ni is introduced in the W powder, sample hardness increases from 4.8 GPa (HMA time = 1 min) to 7.6 GPa (HMA time = 20 min). Fracture resistance of W+5% Ni alloy does not depend on the HMA time and is equal to $\sim$ 5.5 MPa·m$^{1/2}$ (see the Table). Comparison of the findings with the literature data [2] shows that the W+5% Ni alloy hardness is 1.5 to 2 times higher than the hardness of coarse-grain commercial alloys WNiFe-95 and their equivalents.

3. Summary and analysis of the experimental findings

Let's examine the high-speed sintering mechanisms in W and W+5% Ni nanopowders. As shown above, the dependence of powder shrinkage on heating temperature $L(T)$ has a classical three-stage behavior (Figure 4) — low-temperature stage I, where compaction rate is low, intensive shrinkage stage (stage II) and high-temperature stage III, where the powder shrinkage rate is low again [21]. Let's identify the diffusion mechanisms governing the nanopowder compaction process at each SPS stage.

It should be noted preliminary that, in case of SPS, the compacted tungsten and W+5% Ni alloy samples are heated by means of contact heat transmission from the graphite mold. As shown in [7], when electric current flows through the powder, voltage is very high and contact („spot“) area between particles is quite small, factors may be induced that considerably accelerate the metal powder shrinkage process. Such factors, for example, include local particle heating and melting in their contact point (see, for example, [7]). Such conditions are often met in case of high-voltage pulsed electric current consolidation of highly conducting powder materials [22]. In case of low-voltage SPS of tungsten work pieces placed in the graphite mold under pressure, these conditions are rarely met simultaneously. This assumption is in good agreement

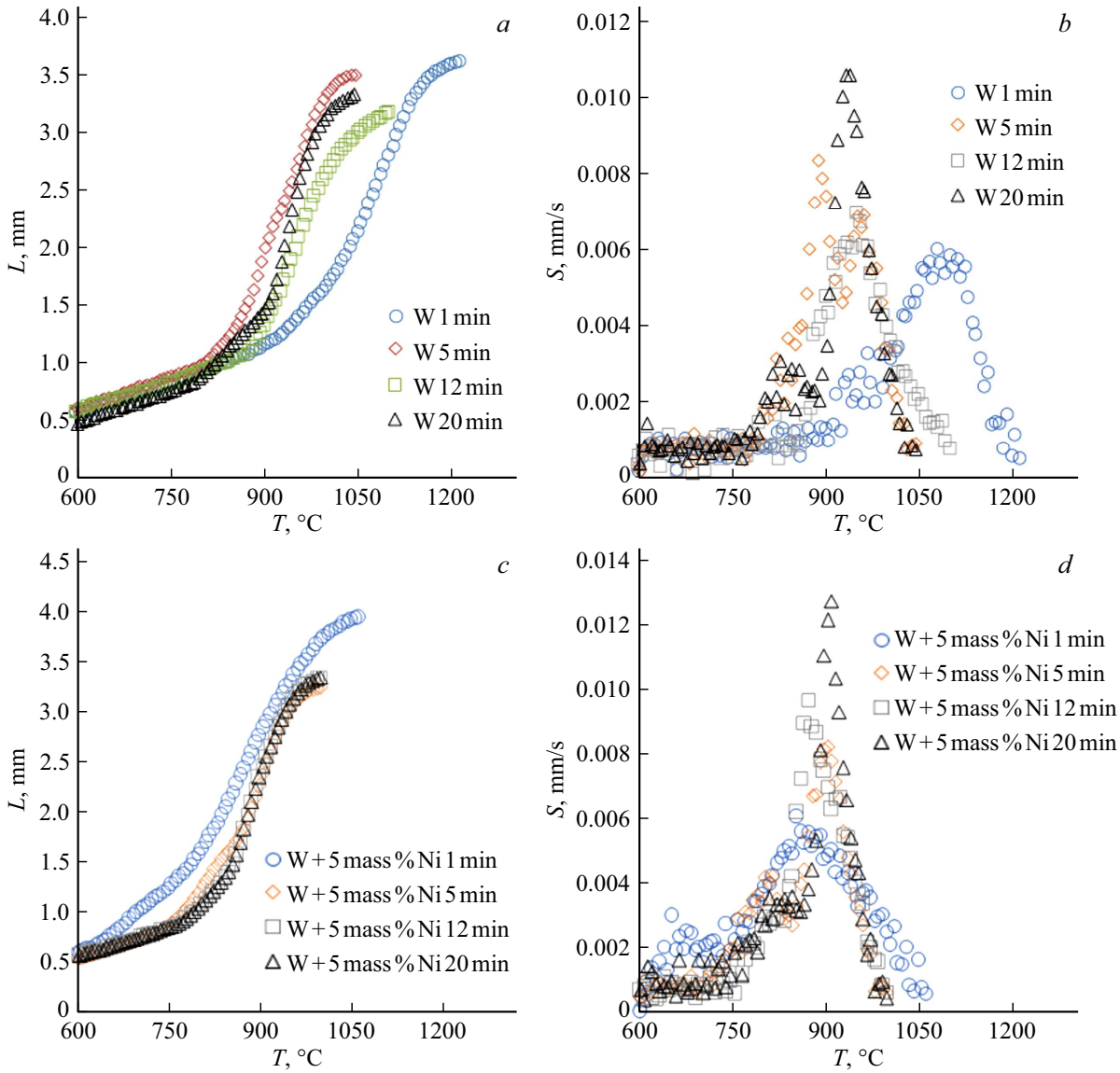

Figure 4. Temperature dependences of shrinkage L (a, c) and shrinkage rate S (b, d) of W (a, b) and W+5% Ni (c, d) powders prepared by the HMA method during various time periods.

Specifications of sintered sample

Composition	HMA time, min	T_2, °C	ρ/ρ_{th}, %	d, μm	Hv, GPa	K_{IC}, MPa·m$^{1/2}$	SPS activation energy		
							Q_{sII}, kT_m	Q_{sIII-1}, kT_m	Q_{sIII-2}, kT_m
W	1	1220	96.6	7.2	3.9	–	6.9	13.7	5.7
	5	1050	96.8	1.8	5.2	5.9	14.4	14.8	5.2
	12	1100	95.8	1.4	5.5	5.3	15.5	9.8	5.6
	20	1050	96.3	0.8	6.5	5.1	10	8.5	5
W+5% Ni	1	1060	99.4	1.8	4.8	–	9	6.7	
	5	1000	98.85	0.5	5.8	5.5	11	7.5	
	12	1000	99.24	0.4	6.9	–	21	8.8	
	20	1000	99.19	0.3	7.6	6.2	12	8.6	

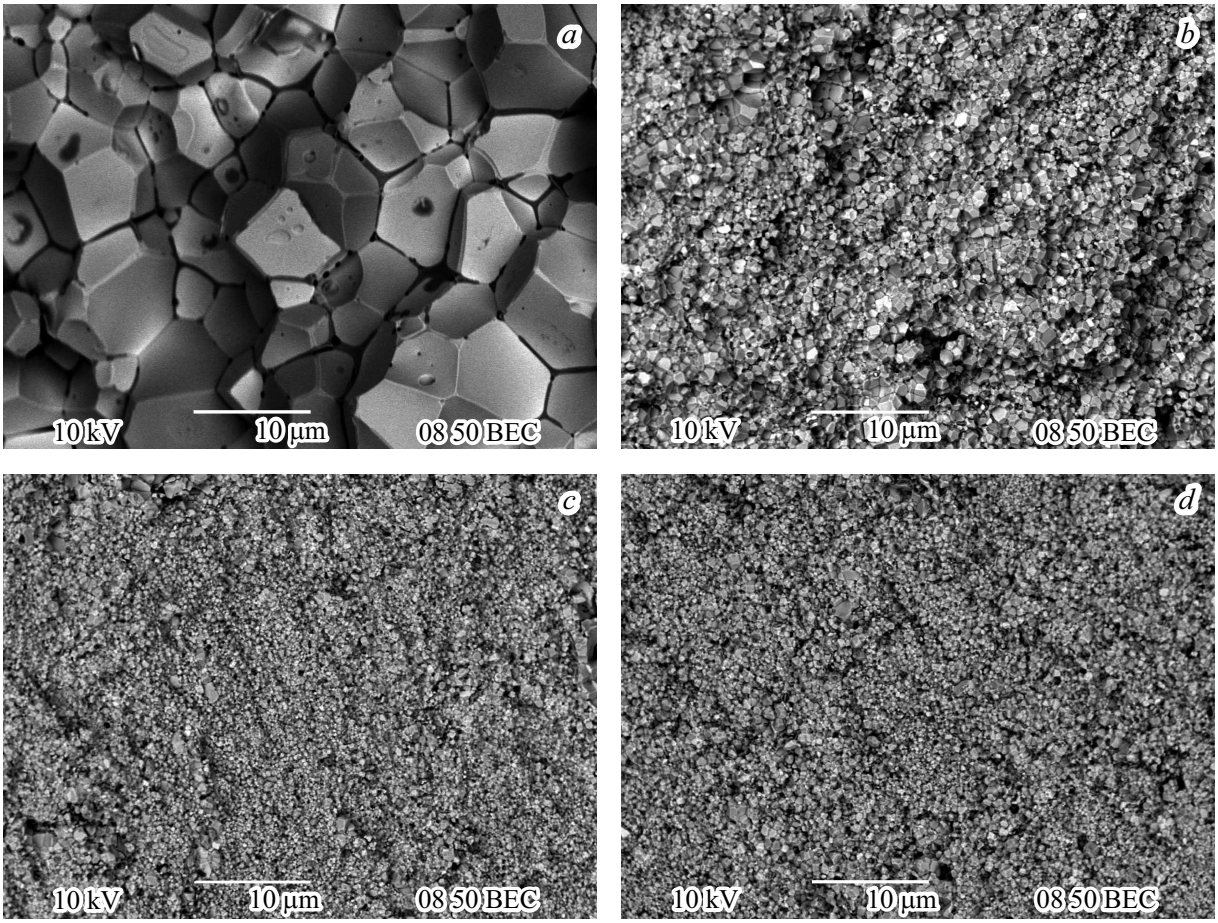

Figure 5. Electron microscopy images of W (*a, b*) and W+5% Ni (*c, d*) samples sintered from powders with various HMA times: *a, c* — 1; *b, d* — 20 min.

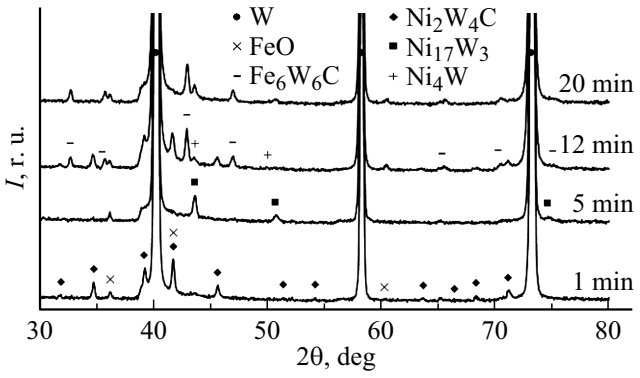

Figure 6. XRD of W samples sintered from powders after various HMA times.

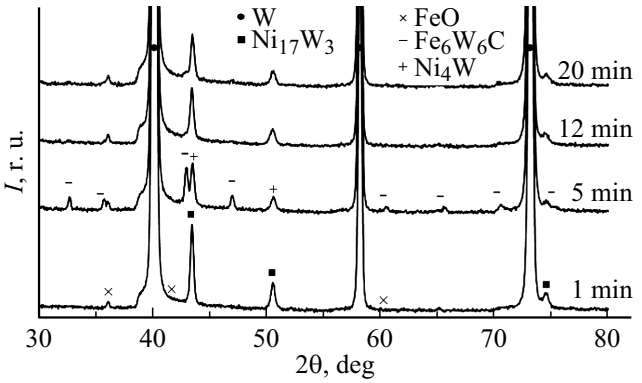

Figure 7. XRD of W+5% Ni alloy samples sintered from powders after various HMA times.

with [23], where such conclusion was confirmed by the case of SPS of micron-size tungsten powders. Non-thermal electric current effect on the tungsten alloy sintering process may be also neglected due to is smallness compared with the temperature and pressure effect [24]. Therefore, to describe the W and W+5% Ni powder compaction process, traditional approaches may be used that are well described in classical literature (see, for example, [21]), as well as the models made to describe the materials sintering process in continuous heating conditions [25,26]. powder compaction kinetics at the intensive compaction stage (stage II) may be analyzed using the Young-Cutler model [25], that describes the initial stage of nonisothermal sintering of spherical particles under conditions of simultaneous bulk and grain-

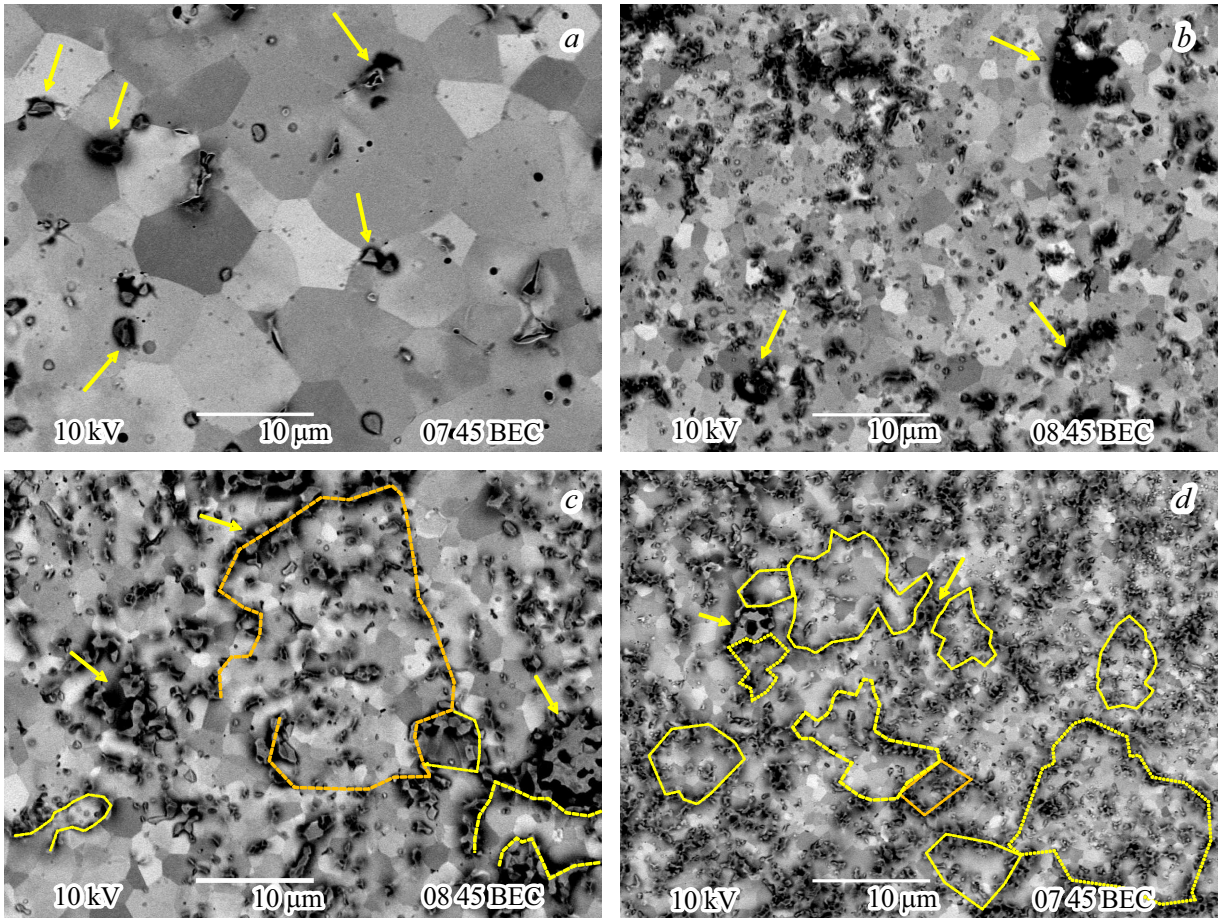

Figure 8. Electron microscopy images of W samples sintered from powders subjected to HMA during 1 (*a*), 5 (*b*), 12 (*c*) and 20 min (*d*); c — dashed lines mark the boundaries of incompletely formed „cells".

boundary diffusion processes, as well as plastic deformation.

$$\varepsilon^2(\partial\varepsilon/\partial t) = (2,63\gamma\Omega D_v\varepsilon/kTd^3) + (0,7\gamma\Omega bD_b/kTd^4) + (Ap\varepsilon^2 D/kT), \quad (1)$$

where ε is the shrinkage, t is the time, γ is the free energy, D_v is the bulk diffusion constant, D_b is the grain-boundary diffusion constant, d is the grain size, p is the pressure, D is the plastic strain diffusion constant. According to [25], the slope of $\ln(T\partial\varepsilon/\partial T) - T_m/T$ corresponds to the effective sintering activation energy mQ_{s2}, where$m$ is the numeric coefficient that depends on the diffusion mechanism ($m = 1/3$ for grain-boundary diffusion case, $m = 1/2$ — for crystal lattice diffusion, $m = 1$ — for viscous flow (creep) of the material, T_m is the material melting temperature).

$\ln(T\partial\varepsilon/\partial T) - T_m/T$ shown in Figure 9 have typical two-stage behavior [25]. Mean effective sintering activation energies at stage II (Q_{sII}) are shown in the Table; effective activation energy Q_{sII} error is ± 0.3 kTm. For plotting $\ln(T\partial\varepsilon/\partial T) - T_m/T$, the pure tungsten melting temperature was taken equal to $T_m = 3695$ K, and the W+5% Ni alloy melting temperature was taken equal to the nickel melting temperature ($T_m = 1726$ K) [1,2].

The Table shows that the effective sintering activation energies were close to the grain-boundary diffusion activation energy [27]. This suggests that the Coble creep process, whose rate is limited by the grain-boundary strain, is the dominating powder compaction mechanism at this stage. This conclusion is in good qualitative agreement with the findings of [11,28–30].

In the high heating temperature region, after a short „transition stage", where the $\ln(T\partial\varepsilon/\partial T)$ variation rate is very low, the slope of $\ln(T\partial\varepsilon/\partial T) - T_m/T$ (Figure 9) becomes negative (stage III). This means that other approaches shall be used to assess the sintering activation energy at stage III.

According to [26], the activation energy at stage III may be assessed using the pore diffusion solution model for pores near the grain boundaries of fine-grain materials. Correct use of this procedure for description of the SPS process of tungsten alloy powders has been demonstrated before in [26,28]. According to the model [26], the sintering activation energy Q_{sIII} is determined by the slope of $\rho(T)/\rho_{th}$ in log-log grid $\ln(\ln(\alpha\cdot\rho/\rho_{th}/(1-\rho/\rho_{th})) - T_m/T$, where$\alpha = 0.33$ is the powder compaction coefficient (Figure 10). Average accuracy of activation energy Q_{sIII} is equal to ± 1 kTm.

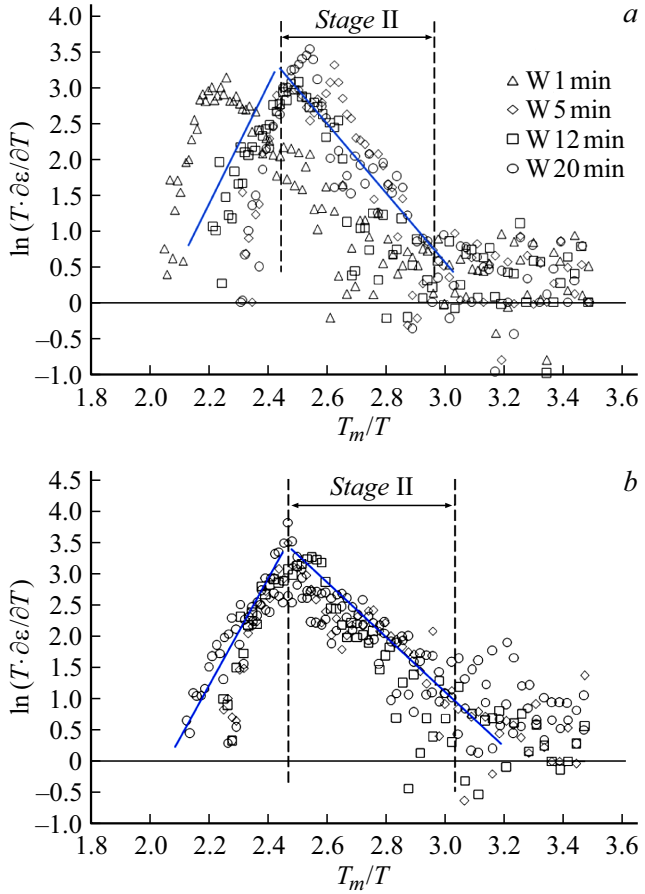

Figure 9. Temperature dependences of shrinkage of W (a) and W+5% Ni (b) powders in coordinates $\ln(T\partial\varepsilon/\partial T) - T_m/T$; a — HMA times are shown.

$\ln(\ln(\alpha\cdot\rho/\rho_{\text{th}}/(\rho/\rho_{\text{th}}-1)) - T_m/T$ for pure tungsten nanopowders at stage III is characterized by a typical kneethat is the evidence of activation energy variation in the „low“ SPS temperature region (stage III-1 with activation energy $Q_{\text{sIII-1}}$) and in the „high“ SPS temperature region (stage III-2 with activation energy $Q_{\text{sIII-2}}$). Increase in the HMA time of tungsten powders results in decrease in the activation energy $Q_{\text{sIII-1}}$ from 13.7 kTm (420 kJ/mol) to 8.5 kTm (280 kJ/mol), that occurs to be slightly lower than the grain-boundary diffusion activation energy of tungsten (380 kJ/mol [27]). We believe that the decrease in the activation energy at stage III-2 may be attributed to formation of grain boundaries with high content of excessive free volume [31] and the start of tungsten particle dissolution in nickel during HMA. Possible causes of decreasing SPS activation energy in mechanically activated nanopowders were discussed in more detail in [8,11,13].

It should be noted that introduction of 5% Ni into tungsten powders results in $\ln(\ln(\alpha\cdot\rho/\rho_{\text{th}}/(1-$ $-\rho/\rho_{\text{th}}-1)) - T_m/T$ behavior variation. For W+5% Ni powders, this dependence is approximated closely by one straight line. The SPS activation energy (Q_{sIII}) of W+5% Ni powders increases slightly from 6.7 kTm (96 kJ/mol) to 8.6 kTm (120 kJ/mol) when the HMA time increases from 1 min, to 20 min. The obtained activation energies are close to the grain-boundary diffusion activation energy of nickel (9 kTm (130 kJ/mol [32])) and to the SPS activation energy at stage II (see the Table). This suggests that the W+5% Ni alloy sintering process in this temperature range is controlled by the Coble creep process intensity by nickel.

Finally, the causes of non-monotonic dependence of the SPS activation energy on the HMA time shall be discussed (see the Table). The Table shows that the SPS activation energy at stage II depends non-monotonically on the HMA time — time increase up to 5–12 min first results in increase in the activation energy Q_{sII}, and with further increase up to 20 min, Q_{sII} decreases again to the values close to the diffusion activation energy at non-equilibrium grain boundaries. It should be also noted that in the higher heating temperature region (stage III), this effect is virtually absent (see the Table).

We believe that the main cause of the observed effect is the formation of strong carbide and intermetallic phases of $Me_xW_yC_z$ and Me_xW_y in this heating temperature range (see the XRD data, Figure 6, 7). At high heating temperatures, the plastic nickel phase enters into high temperature reaction with tungsten, carbon and iron. This, in particular, results in decreasing plastic phase fracture and proportional increase of more strong heat-resistant carbides (Ni_2W_4C) and intermetallic compounds ($Ni_{17}W_3$, Ni_4W). It should be noted that the volume fracture of such coarse micron particles is high (Figure 8) and their hardness exceeds the tungsten and nickel hardness. Large amount of such strong particles in the tungsten alloy microstructure will hinder high-temperature deformation of tungsten and tungsten alloy.

The presence of large amount of strong particles of other phases in the tungsten and W+5% Ni structure will hinder the fine-grain material creep process and, thus, result in increase of the SPS activation energy at stage II. Further increase in the HMA time, on the one hand, results in the

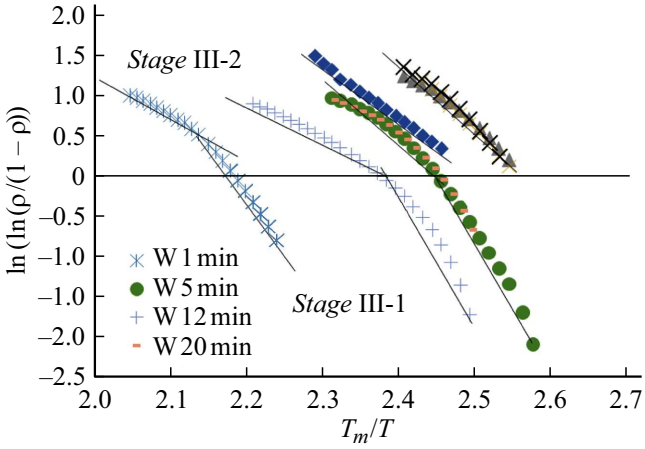

Figure 10. temperature dependences of compaction in coordinates $\ln(\ln(\alpha\cdot\rho/\rho_{\text{th}})/(\rho/\rho_{\text{th}}-1)) - T_m/T$ for powder tungsten and W+5% Ni subjected to various HMA times.

fact that, first, the concentration of carbide and intermetallic particles of $Me_xW_yC_z$ and Me_xW_y in alloys achieves its constant value and then remains virtually unchanged (particle rearrangement and formation of a special „cellular" microstructure are observed (Figure 8, *d*)) and, second, the mean grain size and mean particle size in the sintered alloy decreases with increasing HMA time. This will result in increasing creep rate and decreasing SPS activation energy.

Conclusions

1. The HMA and SPS methods allow to prepare the fine-grain tungsten and W+5% Ni alloy samples. The samples feature high relative density (96.3−99.19%), small grain size (0.3−0.8 μm) and high stress-strain performance. Hardness of tungsten and W+5% Ni samples achieves 6.5 GPa and 7.6 GPa, respectively, and the minimum Palmquist fracture resistance coefficient for these alloys is equal to 5.1 and 6.2 MPa·m$^{1/2}$. Hardness of the prepared fine-grain samples is 1.5 to 2 times higher than the hardness of commercial coarse-grain tungsten alloys.

2. High-speed sintering mechanisms in mechanically activated W and W+5% Ni nanopowders have been defined. The causes of pulsed electric current sintering of mechanically activated W nanopowders and W+5% Ni powder composition include, first, decrease in the initial particle sizes, second, formation of grain boundaries with high content of excessive free volume during HMA, third, tungsten particle dissolution in the plastic nickel phase surrounding the strong W particles. Combined effect of these factors results in increasing grain-boundary diffusion intensity and, thus, in increasing Coble creep rate.

3. It has been shown that carbide and intermetallic phases of $Me_xW_yC_z$ and Me_xW_y are formed in alloys during SPS primarily as a result of contamination with foreign impurities from the steel balls and container. Formation of carbide and intermetallic phases results in non-monotonic variation of the SPS activation energy when the HMA time increases in the „intermediate" heating temperature region (intensive powder shrinkage region). In the „high" heating temperature region, the SPS activation energy is weakly dependent on the HMA time and is close to the grain-boundary diffusion activation energy.

Funding

The study was supported by RSF grant No. 22-79-10080.

Conflict of interest

The authors declare that they have no conflict of interest.

References

[1] E.C. Green, D.J. Jones, W.R. Pitkin. Symp. Powder Met., **58**, 253 (1954).

[2] J. Das, G.A. Rao, S.K. Pabi. Mater. Sci. Eng. A, **527** (29−30), 7841 (2010). DOI: 10.1016/j.msea.2010.08.071

[3] U. Ravi Kiran, A. Sambasiva Rao, M. Sankaranarayana, T.K. Nandy. Int. J. Refract. Hard. Met., **33**, 113 (2012). DOI: 10.1016/j.ijrmhm.2012.03.003

[4] G. Parabhu, N.A. Kumar, M. Sankaranarayana, T.K. Nandy. Mater. Sci. Eng. A, **607**, 63 (2014). DOI: 10.1016/j.msea.2014.03.130

[5] P.V. Krasovskii, A.V. Samokhin, A.A. Fadeev, M.A. Sinayskiy, S.K. Sigalev. J. Alloys Compd., **250**, 265 (2018). DOI: 10.1016/j.jallcom.2018.03.367

[6] M. Tokita. Ceramics, **4** (2), 160 (2021). DOI: 10.3390/ceramics4020014

[7] E. Olevsky, D. Dudina. *Field-Assisted Sintering* (Springer Int. Publ., 2018), DOI: 10.1007/978-3-319-76032-2

[8] V.N. Chuvildeev, D.V. Panov, M.S. Boldin, A.V. Nokhrin, Yu.V. Blagoveshchensky, N.V. Sakharov, S.V. Shotin, D.N. Kotkov. Acta Astronaut., **109**, 172 (2015). DOI: 10.1016/j.actaastro.2014.11.008

[9] L. Ding, D.P. Xiang, Y.Y. Li, C. Li, J.B. Li. Int. J. Refract. Hard. Met., **33**, 65 (2012). DOI: 10.1016/j.ijrmhm.2012.02.017

[10] D.P. Xiang, L. Ding, Y.Y. Li, G.B. Chen, Y.W. Zhao. J. Alloys Compd., **562**, 19 (2013). DOI: 10.1016/j.jallcom.2013.02.014

[11] V.N. Chuvil'deev, A.V. Nokhrin, M.S. Boldin, G.V. Baranov, N.V. Sakharov, V.Yu. Belov, E.A. Lantsev, A.A. Popov, N.V. Melekhin, Yu.G. Lopatin, Yu.V. Blagoveshchenskiy, N.V. Isaeva. J. Alloys Compd., **773**, 666 (2019). DOI: 10.1016/j.jallcom.2018.09.17

[12] X. Li, H. Xin, K. Hu, Y. Li. Transactions of Nonferrous Metals Society of China, **20**, 443 (2010). DOI: 10.1016/S1003-6326(09)60160-6

[13] A.M. Bragov, V.N. Chuvil'deev, N.V. Melekhin, A.R. Filippov, A.Y. Konstantinov, N.V. Sakharov. Phys. Mesomech., **22**, 307 (2019). DOI: 10.1134/S1029959919040064

[14] A.V. Nokhrin, N.V. Malekhonova, V.N. Chuvil'deev, N.V. Melekhin, A.M. Bragov, A.R. Filippov, M.S. Boldin, E.A. Lantsev, N.V. Sakharov. Metals, **13** (8), 1432 (2023). DOI: 10.3390/met13081432

[15] E. Lang, A. Kapat, T.W. Morgan, J.P. Allain. J. Nucl. Mater., **544**, 152672 (2021). DOI: 10.1016/j.jnucmat.2020.152672

[16] L.A. El-Guebaly, W. Setyawan, C.H. Henager Jr, R.J. Kurtz, G.R. Odette. Nucl. Mater. Energy., **29**, 101092 (2021). DOI: 10.1016/j.nme.2021.101092

[17] R. Neu, H. Maier, M. Balden, S. Elgeti, H. Gietl, H. Greuner, A. Herrmann, A. Houben, V. Rohde, B. Sieglin, I. Zammuto, ASDEX Uprade Team. Fusion Eng. Des., **124**, 450 (2017). DOI: 10.1016/j.fusengdes.2017.01.043

[18] T. Laas, K. Laas, J. Paju, J. Priimets, S. Tõkke, B. Väli, V. Shirokova, M. Antonov, V.A. Gribkov, E.V. Demina, V.N. Pimenov, M. Paduch, R. Matulka, M. Akel. Fusion Eng. Des., **151**, 111408 (2020). DOI: 10.1016/j.fusengdes.2019.111408

[19] A.A. Mazilkin, B.B. Straumal, S.G. Protasova, M.F. Bulatov, B. Baretzky. Mater. Lett., **192**, 101 (2017). DOI: 10.1016/j.matlet.2016.12.049

[20] E.A. Lantsev, N.V. Malekhonova, Y.V. Tsvetkov, Yu.V. Blagoveshchensky, V.N. Chuvildeev, A.V. Nokhrin, M.S. Boldin, P.V. Andreev, K.E. Smetanina, N.V. Isaeva. Inorg. Mater. Appl. Res., **12**, 650 (2021). DOI: 10.1134/S2075113321030242

[21] M.N. Rahaman. *Ceramic Processing and Sintering.* 2nd ed. (Marcel Dekker Inc., NY., 2003)

[22] E.G. Grigoriev. *Sb. materialov konferentsii „Aktualnye Problemy Poroshkovogo Materialovedeniya"* (Perm, 2018), s. 25. (in Russian)
[23] S. Deng, H. Zhao, R. Li, T. Yuan, L. Li, P. Cao. Powder Technol., **359**, 769 (2019). DOI: 10.1016/j.powtec.2019.08.108
[24] S. Deng, R. Li, T. Yuan, P. Cao. S. Xie. Metall. Mater. Trans. A., **50**, 2886 (2019).
[25] W.S. Young, I.B. Culter. J. Am. Ceram. Soc., **53**, 659 (1970). DOI: 10.1111/j.1151-2916.1970.tb12036.x
[26] V.N. Chuvil'deev, Y.V. Blagoveshchenskiy, A.V. Nokhrin, M.S. Boldin, N.V. Sakharov, N.V. Isaeva, S.V. Shotin, O.A. Belkin, A.A. Popov, E.S. Smirnova, E.A. Lantsev. J. Alloys Compd., **708**, 547 (2017). DOI: 10.1016/j.jallcom.2017.03.035
[27] L.N. Larikov, Yu.F. Yurchenko. *Diffusion in Metals and Alloys* (Naukova dumka, Kiev, 1987)
[28] L.S. Golovkina, A.I. Orlova, A.V. Nokhrin, M.S. Boldin, V.N. Chuvil'deev, N.V. Sakharov, O.A. Belkin, S.V. Belkin, A.Yu. Zelenov. Mater. Chem. Phys., **214**, 516 (2018). DOI: 10.1016/j.matchemphys.2018.03.091
[29] G. Lee, J. McKittrick, E. Ivanov, E.A. Olevsky. Int. J. Refract. Met. Hard Mater., **61**, 22 (2016). DOI: 10.1016/j.ijrmhm.2016.07.023
[30] S. Deng, J. Li, R. Li, H. Zhao, T. Yuan, L. Li, Y. Zhang. Int. J. Refract. Met. Hard Mater., **93**, 105358 (2020). DOI: 10.1016/j.ijrmhm.2020.105358
[31] Yu.R. Kolobov, G.P. Grabovetskaya, K.V.'Ivanov, N.V. Girsova. Phys. Metals Metallography, **91**, 532 (2001). (in Russian)
[32] V.N. Chuvildeev. *Neravnovesnye granitsy zeren v metallakh. Teoriya i prilozheniya* (Fizmatlit, M., 2004) (in Russian)

Translated by Ego Translating